Aerodynamic design and development of the Sunswift IV solar racing car

Graham Doig*

School of Mechanical and Manufacturing Engineering,
The University of New South Wales,
Sydney, NSW 2052, Australia
E-mail: g.doig@unsw.edu.au
*Corresponding author

Chris Beves

CD-adapco,
200 Shepherds Bush Road,
London W6 7NL, UK
E-mail: cbeves@hotmail.com

Abstract: The aerodynamic design and development of the University of New South Wales' ultra-low-drag solar-electric Sunswift IV car is described, detailing the student-led design process from initial concept sketches to the completed vehicle. The body shape was established and refined over a period of six months in 2008–2009, almost entirely using computational fluid dynamics. The guiding philosophy was that predictable handling and drag minimisation in challenging, changing wind conditions of the type commonly seen during the World Solar Challenge across Australia was preferable to high performance only on 'perfect' days. The car won its class in the 2009 and 2011 World Solar Challenges, and holds the Guinness World Record for fastest solar-powered vehicle.

Keywords: CFD; computational fluid dynamics; solar car; aerodynamics; land speed record; streamlining; world solar challenge; renewable energy; ground effect; vehicle design.

Biographical notes: Graham Doig is a Lecturer at the University of New South Wales (UNSW). He received his MEng from the University of Glasgow and his PhD UNSW, and subsequently worked as a mechanical engineer for AECOM. His current research areas include automotive aerodynamics and high speed flows. He was Aerodynamics Team Leader for the group which designed the Sunswift IV solar car, and initiated the land speed record project – he is currently academic supervisor to the present Sunswift team.

Chris Beves received his BEng and PhD from the University of New South Wales in 2004 and 2009, respectively. He currently works as a consultant at CD-adapco in London, specialising in using computational fluids dynamics

to deliver solutions to the Automotive, Aerospace and Oil and Gas Industries. Chris was Lead Aerodynamicist for the design of Sunswift IV, and also consulted extensively to the mechanical design team.

1 Introduction

Motivated by ever-increasing fuel prices, and acute public awareness of climate change issues and the considerable role transportation plays in contributing to carbon emissions, much private and industry interest has been focused on alternative energy vehicles in the last quarter of a century. Despite occupying a highly niche area of motorsport, solar-electric prototype racing has captured public imagination thanks largely to an emphasis on highly unusual (and aerodynamic) design and the fanfare of zero-emissions cross-continental races, particularly in the USA and Australia. Despite the majority of projects past and present being developed at universities as student-led projects, the teams often attract high-technology corporate involvement both as partners and sponsors.

While a true commercial solar-electric hybrid is presently unfeasible due to limited solar panel efficiency and the current cost of arrays, these vehicles are effective technological demonstrators for electric motor, battery and solar cell technology. They have also served as a training ground for thousands of engineers.

Given that around 70% of all the power from the solar array is used to overcome air resistance, as illustrated in Figure 1, effective streamlining is paramount. The approximate rolling resistance shown was deduced from roll-down testing as described in literature (Boulgakov, 2011), and pales in comparison. However, precisely because the vast majority of these projects are undergraduate-based, little publicly-available information exists on the aerodynamic aspects of a modern solar racing car and the design process. The reader interested in history and evolution of solar car design concepts is directed towards Tamai's comprehensive 'The Leading Edge', although that reference mostly predates the present ubiquity of computational fluid dynamics (CFD). This paper describes in detail the computationally-led aerodynamic design and development of the successful Sunswift IV vehicle. While a handful of technical, refereed descriptions of aerodynamic studies of solar cars exist in the public domain (Himeno and Matsubara, 1994; Cusack et al., 1997; Yang and Liou, 2005; Hoerl et al., 2008; Taha et al., 2011), they tend to be brief and the numerical methods, particularly with regards to mesh quality and the accuracy of the results, are of disputable reliability due to resource constraints and a lack of good validation data.

The modern era for solar cars began in 1987 with the inaugural World Solar Challenge (WSC), a rally race from Darwin to Adelaide in Australia, covering 3021km (1877 miles) which continues to be run every two years. The race followed on from the pioneering work of Hans Thostrup and the car 'The Quiet Achiever', engineered by Larry and Gary Perkins, which completed a landmark Sydney to Perth journey in under 20 days in 1983 with an 8.5 m^2 array producing approximately 1 kW of power.

Progress in vehicle performance experienced remarkable growth during the heyday of solar racing, from 1987 until approximately a decade and a half later when race times in the WSC hit a ceiling owing to cars travelling at or close to the speed limit in the Northern Territory and South Australia. Rules have become increasingly restrictive to promote greater safety and to force teams to continue to make efficiency gains by cutting

their available solar and battery capacity. A handful of selected vehicles, with their performance and achievements, are summarised in Table 1, highlighting the evolution of performance; as solar arrays have reduced in size, average race and top speeds have generally increased. With much of the technology now mature, the main frontier for such vehicles is now progress in batteries, pending breakthroughs in low-cost cell efficiency.

Figure 1 Example of power required to overcome rolling and aerodynamic resistance, loosely based on Sunswift IV
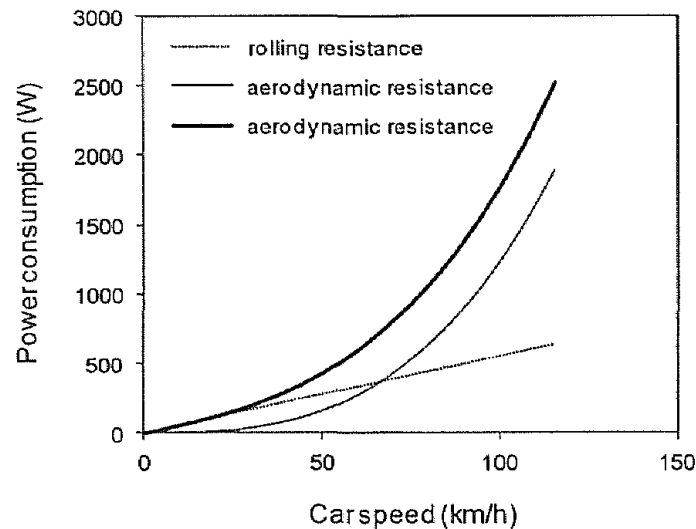

Table 1 Selected solar racing cars with relevant performance details and achievements

Vehicle	Weight	Array type/power	Array area	Achievements
The Quiet Achiever	150 kg	~1kW	8.5 m²	First Australian transcontinental crossing by a solar vehicle, *1983* (average speed 24 km/h)
GM SunRaycer	265 kg	~1.5kW	9 m²	Winner of inaugural WSC *1987*, (average speed) 67 km/h
Honda Dream	167 kg	Silicon/1.9kW (~23% efficiency)	9.4 m²	Winner, *1993* WSC (average speed 84 km/h)
Nuna 3	<200 kg	Gallium-arsenide/ 2.3 kW+ (~27% efficiency)	8 m²	Winner, WSC *2005* (average speed 103 km/h)
Sunswift IV	164 kg	Silicon/~1.3 kW (~22% efficiency)	6 m²	Winner (silicon class) WSC *2009* (average speed 77 km/h, Guinness Land Speed Record Holder (*2011*), 89 km/h Winner (Production Class) WSC 2011

Rules for 2011 (International Solarcar Federation, 2010), designed to curb performance and promote continued innovation, dictated that the driver must be sitting relatively upright at 27° from vertical (primarily for safety reasons, to eliminate designs with a

driver lying near-flat in the body of the car as were standard in previous years). A maximum of 6 m² of silicon array was permitted, or 3 m² of more efficient – but more expensive – gallium arsenide cells. In this climate of regulations, and following the race-winning success of similar designs from the Delft University of Technology 'Nuna' team (winners 2001, 2003, 2005, 2007) and the Japanese Tokai team (winners 2009, 2011), designs of solar cars at the competitive end of the field have homogenised remarkably compared to the earlier days of the event when wildly-different designs raced (Tamai, 1999; Roche et al., 1997). The non-dimensional drag coefficient based on frontal area, C_{DX}, of current leading designs tends to be around or even less than 0.1 (Tamai, 1999); a significant change to regulations would be required to reverse the trend towards very standard designs. Almost all successful cars from the last decade featured three wheels with two steering fronts and the driver sitting close to the rear (powered) wheel in a single large 'bumpod' fairing.

Sunswift IV is a three-wheeled vehicle in this configuration, with the driver seated close to the rear of the vehicle to allow undisturbed airflow over the upper surface of the main body (and to minimise any shading from the canopy onto the solar array). A brushless DC motor is embedded into the rear drive wheel, eliminating the need for a mechanical drive train. The body is a carbon fibre monocoque chassis, which forms both the supporting frame for the car's systems and its outer aerodynamic shape (Boulgakov, 2011). The top half of the body is not strictly structural, but gives support and contour to the solar array. The car is controlled with two hand-operated throttles mounted to the steering wheel: one for acceleration and one for regenerative braking. A foot-operated mechanical braking system exists for emergency use. The car is equipped with a 21 kg lithium ion battery pack which is able to store about 5 kWh of energy (approximately enough to power the car at 80 km/h for 5 h), and three maximum-power-point trackers ensure that the energy collected from the 1.3kW array is efficiently stored (Boulgakov, 2011).

## 1.1 The Sunswift project, and Sunswift IV design philosophy

Sunswift originated at the University of New South Wales in the mid-1990s, conceived as a student-led project. It remains as an endeavour on which students gain unique hands-on experience in all areas of design, from mechanical to electrical to aerodynamic, and beyond to marketing and finance. Sunswift II was the first vehicle to be designed by the students, who became the first and only team to incorporate their own solar cells; the shape of the car was influenced by computational fluid dynamics (CFD). Sunswift III was designed for the 2005 WSC, using CFD and some wind tunnel testing of components such as wheel fairings, and also raced in 2007 with some minor modifications. It broke the long-standing transcontinental record from Perth to Sydney in a new time of 5.5 days.

Sunswift IV was built in 2008/2009. The aerodynamic design team was briefed to take the vehicle from sketch-pad concept to design freeze configuration (Figure 2) in a period of around 5 months. This allowed time for a tight 8-month build program ahead of the October 2009 World Solar Challenge. The timeframe and budget considerations instantly precluded the use of a wind tunnel, thus rapid digital design was embarked upon, commencing in August 2008.

The team's goal was to create a car featuring low-drag performance over as wide a range of operating conditions as possible, as the car had to drive in the real world rather than the 'perfect' conditions of a wind tunnel or in the digital domain.

Therefore designing a well-rounded – literally as well as figuratively – shape for viable aerodynamic stability was paramount, given that cross winds and gusts constantly subject the car to relatively high loads. These are very influential to a light car based on a wing section body. Several of the 2009 and 2011 cars had notably thin body profiles with relatively angular side rails compared to cars in previous years – in windy conditions these facets would promote the kind of force sensitivity and flow separation which Sunswift wished to avoid.

Figure 2 Initial concept sketch, and the final vehicle as completed less than 12 months later
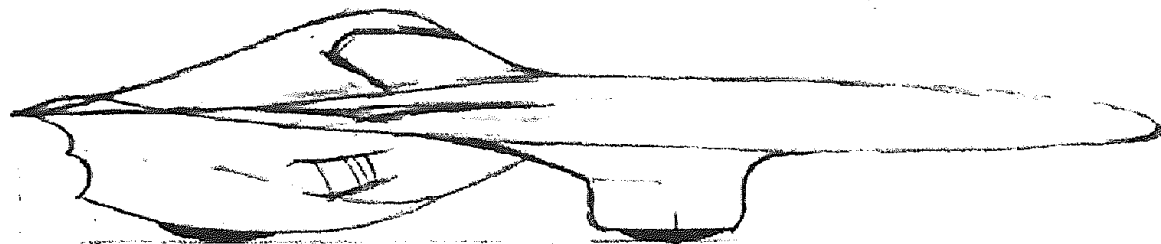
(a)

(b)

Source: Photo: Matt Cumming

The ideal scenario for any solar car is to hold a constant speed (Pudney, 2000); if Sunswift IV were to travel at 80 km/h for one hour it would use around 1050 Wh of energy, whereas if it were to travel at 60 km/h for the first 30 min and 100 km/h for the remainder of the hour, it would average the same speed but use 11% more energy. Therefore a car that can hold speed and momentum over undulating terrain (Arkesteijn et al., 2007), and maintain low aerodynamic drag when there are changing wind conditions will maximise the available power during long stretches of driving.

Given the dominant success of the Nuna team with essentially-similar designs from 2001–2007, their general design was used as a template on which to not only improve along the lines of the philosophy outlined above, but also add some unique, slightly theatrical aerodynamic touches to create an attractive vehicle which would help generate publicity and sponsorship. Hanging the rear of the canopy and bumpod back beyond the main body wing section (as can be seen in Figure 2) was not only done for aesthetics but to facilitate one of the more important design features of the car; in combination with curving back the wing tip trailing edges in the so-called 'batwing' configuration,

this provided the airflow with three distinct points at which to detach from the body. Controlling the separation from the car somewhat in gusty conditions was deemed essential for handling, performance and safety. Similarly, the generally curvaceous nature of the leading edge and side rails of the main body were designed to meet and guide flow coming from most realistic angles.

A silicon array was necessary to keep costs down, leading to a predicted maximum power output of around 1.2 kW. A decision was made to retain the effective front wheel fairing design from Sunswift III, but otherwise free reign was given to the aerodynamic team. The total cost of designing, building and racing the vehicle (cash and in-kind), including the array, was approximately $350,000 AU, compared to the US$500,000 to $1m+ budgets of 2009 and 2011 competitor vehicles from the University of Michigan, Delft University of Technology and Tokai University.

A simple approach was conceived for the aerodynamic development, whereby enough parametric runs would be conducted to infer or interpolate an approximate optimum for each major body part. Therefore, parametric studies were carried out relating to the longitudinal position and shape of the canopy and bumpod to determine how far back these could be placed while maintaining high performance of the car. The wheel faring position was also analysed to examine the relationship between this and performance of the bumpod. These studies were conducted with a basic configuration (relatively thick body section, simplified shapes), with a final aeromap of the refined car generated for both normal and yawed conditions at various car and wind speeds at the end of the development timeline.

It is worth noting that many of the aerodynamic gains being chased were very small – it is not a complex task to design a simple car around low-drag aerofoil shapes that will do a workman-like job. However, when compounded over the course of four to five days of racing, a few drag counts can make a considerable difference, and therefore careful incremental optimisation was a valuable exercise.


2 Numerical method

Dassault Systems' CATIA software was used to develop the CAD models, and ANSYS Fluent (v6.3) was used to solve the CFD on a parallel cluster. The node-based, segregated pressure solver was used, with convergence deemed acceptable at a point, after close to 1000 iterations, at which the aerodynamic coefficients ceased to change by more than 1% with a further 1000 iterations. The approach to meshing and convergence was derived from a combination of experience and experimentation with settings to achieve a good balance between solution time and accuracy.

All computational meshes were created using ANSYS Workbench in order to take advantage of a certain amount of automation. Significant attention in meshing was paid to areas of high geometric curvature or complexity, such that minimal faceting of the surface was present. The node spacing away from the vehicle was coarsened relatively rapidly to keep the total number of cells down; such an approach is justified for this type of vehicle, as the pressure disturbances do not extend far from the body, and separation ought to be minimal. The mesh was tightly controlled in the wake regions of the front wheel fairings and the main body of the car, to ensure adequate capture of vortex behaviour and thus avoid significant over-estimation of drag. A hybrid approach of prism mesh clustered close to the surfaces of the car and tetrahedral mesh to the far-field

allowed the boundary layers to be well-resolved and Fluent's non-equilibrium near-wall model to be implemented (Fluent Inc., 2006) to improve accuracy in viscous drag prediction. Some examples of the mesh density and structure on a mid-plane through the vehicle model are shown in Figure 3.

Figure 3   (a) The CFD mesh on the symmetry plane around the full car, with detail at the leading edge and canopy and (b) a schematic of the total domain for symmetric (zero yaw) cases
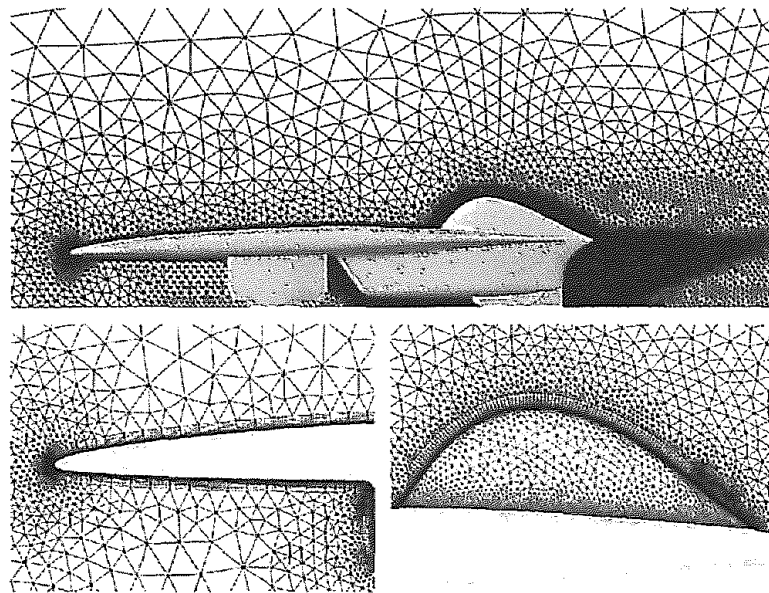
(a)
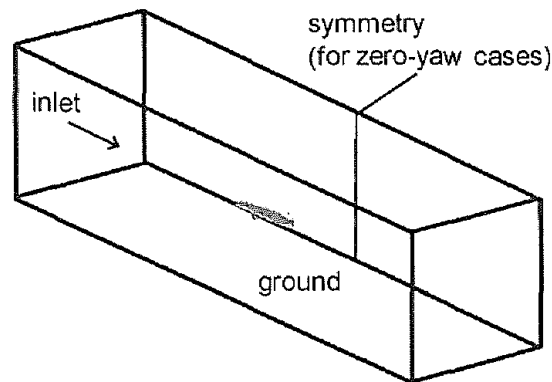
(b)

True mesh convergence was not possible due to time and computational resource constraints. This was not deemed vital as the majority of the design study was parametric and thus like-for-like comparisons were sufficient in the earlier stages. For the finished design, a simulation was run with a mesh featuring approximately 1.5 times the mesh resolution in all regions, which was found to affect lift by less than 3%, and drag by less than 5% – primarily a result of a change in the predicted value of viscous drag due to improved resolution in the boundary layer; pressure drag increased by a minimal amount. Therefore the standard mesh of approximately 6.5×10^6 cells for a symmetry (half car) model and 13×10^6 cells for a full car model was deemed acceptable for the final iterations of the design. Approximately half these values were sufficient

for the simplified initial models for the parametric studies, as they did not feature the wheel/ground interaction or areas of complex curvature introduced in the latter configurations.

The boundary conditions were as follows: a velocity inlet 8 m upstream of the car leading edge, with a zero-pressure outlet 20m downstream. Other outlets were positioned 7 m from the vehicle. These locations were determined, from a simple analysis on a representative NACA 66-series aerofoil, to be sufficiently clear of the vehicle to exert negligible influence on the solution. For clarity the boundaries are shown in Figure 3, and cases with the full car featured double this domain in the lateral direction.

The ground was set to be a zero shear wall, as opposed to a moving ground which would ordinarily be the correct boundary condition to reproduce real world conditions. The simplification allowed a more simplistic meshing of the ground. Though a ground boundary layer would form under the car due to the minor pressure gradient caused by the car and in particular the wheels (Barber et al., 2002), it would be very small in relation to the car's total ground clearance, and furthermore the wheel/ground contact patch was simplified to avoid unwanted inherent unsteadiness showing up in the simulation. Accurate modelling of the ground would be wasteful given the reduced geometric complexity of the wheel. Airflow inside the wheel well was not considered, and it was assumed that with such a small portion of the wheel exposed to the oncoming air, the wheel rotation would not have been a significant influence on the wake as it would be for a fully-exposed wheel (Diasinos, 2009).

From the results of simulations on the NACA section (Abbott and von Doenhoff, 1959) and extensive local experience in simulating aerodynamic aspects of racing cars, the Realisable $k-\varepsilon$ turbulence model was chosen for all runs (Shih et al., 1995). This model has been used in several recent validated numerical studies for motorsport applications – with a similar mesh density – to good effect for wings and wheels (McManus and Zhang, 2006; Doig and Barber, 2011; Doig et al., 2011; Diasinos et al., 2013), and therefore was expected to be reliable. Testing with additional models was not practical in the given timeframe, particularly given a lack of physical test data to validate against; some testing after the fact with other models did not yield any data which would have altered the design process described here. While a good run of laminar flow was the primary reason for using the NACA-66 series as a base for the car body, laminar to turbulent transition remains a difficult proposition for Reynolds-Averaged Navier–Stokes CFD and would have required a significantly finer and more consistent mesh on the car than was feasible.

It is anticipated that a laminar run of as much as 30% of the upper surface, and on the lower surface to at least the chordwise location of the front wheel fairings, would be present in 'perfect' conditions (Tamai, 1999), and thus actual drag values would be less than those predicted by the fully-turbulent CFD due to significantly decreased skin friction. In the race, however, any laminar flow is likely to be more limited and intermittent; a build up of dust and insects, combined with constantly changing wind conditions and the effect of bumps in the road on a very light car with relatively crude suspension, all add up to a transient, sensitive laminar region likely to make a much smaller contribution to drag reduction than is typically cited (Tamai, 1999). However, it is also worth noting that a turbulent boundary layer over the solar array promotes greater heat transfer and thus better cooling, so there is a trade-off to be made.

The following sections present an overview of the parametric design process – we present only the most indicative configurations from the hundreds of combinations that

were investigated. Most runs were conducted at 25 m s^{-1} and 35 m s^{-1}, corresponding roughly to cruising and top speed respectively. Note that force coefficients are expressed as non-dimensional and as a function of the relevant area (projected plan area for lift, frontal area for drag, and side area for side force).

3 Cockpit canopy

The cockpit design focused largely on the canopy placement along the length of the car, how long it should be, and what fineness (length to width ratio) ratio would be optimal. The frontal area had to be large enough to accommodate a helmet, determining the width, and a race-legal roll hoop determined the height.

The main wing section was 'locked in' such that the driver's shoulders were covered, to satisfy the rule that the chassis rails form part of the driver protection cell. The main wing was placed initially at zero incidence and as far away from the ground as was practical, to minimise the 'ground effect' influence such a large wing would have. This would avoid both a drag augmentation and an increase in pitch sensitivity due to ground proximity. At first, a worst case bumpod was used (i.e., long and wide, relatively constant cross section).

Geometric parameters are outlined in Figure 4, followed by total vehicle lift and drag coefficient values obtained, in Table 2, for selected configurations at a cruising speed of 25 ms^{-1} (90 km/h) and a top speed of 35 ms^{-1} (126 km/h). The fillet at the canopy/body joint was adjusted to eliminate any separation at the leading edge of the windscreen. Note that the total drag values are artificially low as the wheels and front wheel fairings were not included in the model at this stage.

Figure 4 Parameters for canopy and bumpod optimisation studies on a simplified chassis
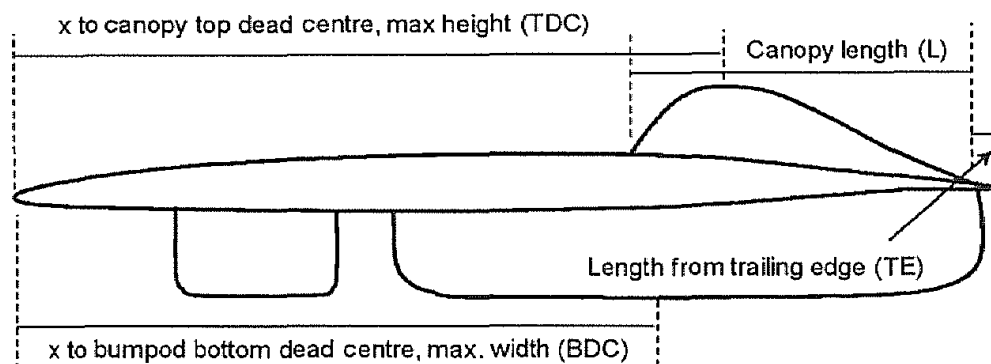

Table 2 Total vehicle lift and drag coefficients and efficiency for the canopy configurations presented in Figures 5 and 6

Case (TDC-L)	25 ms^{-1}			35 ms^{-1}		
	C_D	C_L	L/D	C_D	C_L	L/D
2650–1800	0.116	0.121	1.04	0.108	0.118	1.09
2650–2000	0.116	0.119	1.02	0.108	0.133	1.23
2900–1400	0.117	0.126	1.08	0.110	0.122	1.12
3150–1300	0.117	0.085	0.72	0.109	0.081	0.74

The curvature of the canopy relative to the oncoming flow produces low pressure relative to the rest of the vehicle, ensuring a lifting contribution. Although this is enough to ensure the vehicle will always have a nose-down pitching moment, which is a vital stability and safety issue, too much lift would produce excessive pressure gradients (and therefore increased drag) and reduce the stability in winds by introducing volatility in flow separation. Some indicative canopy geometries with pressure and turbulent kinetic energy contours are shown in Figures 5 and 6, for a car speed of 25 ms^{-1} – a sharp reduction in kinetic energy indicates a greater propensity towards separation, and a strong pressure gradient will lead to this as well as increasing the forces acting on the surface.

Figure 5   Example of 'short' canopy configurations, pressure coefficient and turbulent kinetic energy surface contours. Quoted lift and drag values are for the canopy only (see online version for colours)
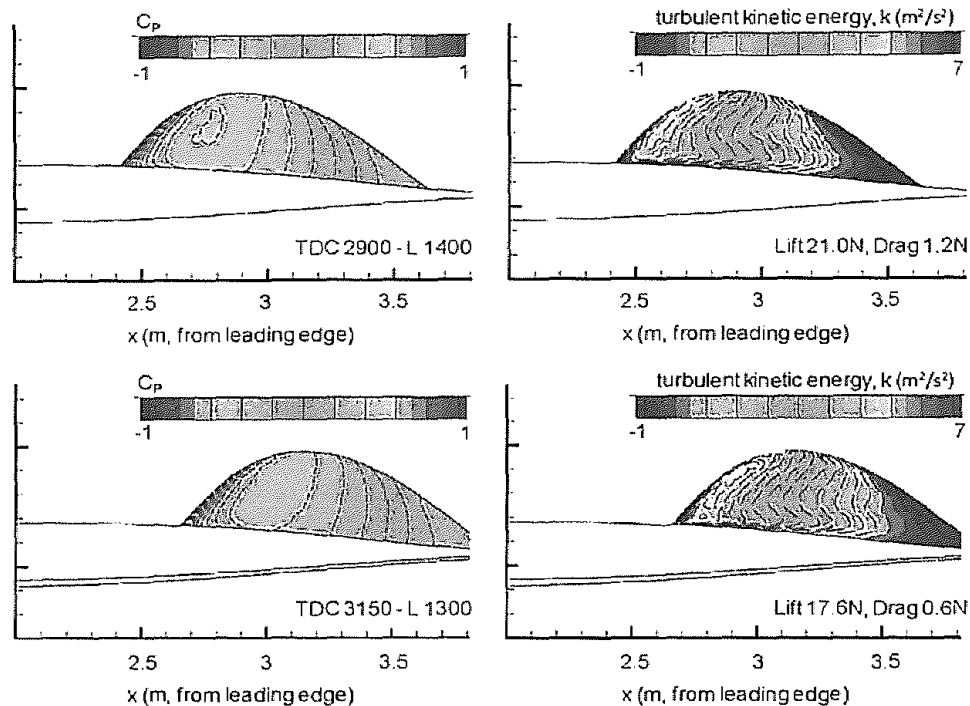

Identical shapes of canopy indicated that the placements further to the rear of the car reduced total drag by up to 20% compared to the most forward location owing to less interference from the wing pressure gradient, and reduced total lift by as much as 50% by shifting the canopy low pressure away from where it combines with the peak suction on the main body. This is illustrated by the contour plots of the similar canopies shown in Figure 5. Reducing the angle of the front of the canopy also serves to reduce pressure gradients and therefore drag – this can be seen in Figure 6 by comparing the 2650–1800 example with the 2650–2000 iteration, with particular emphasis on the reduced turbulent kinetic energy (and pressure gradient) at the canopy leading edge that essentially halves the total canopy drag.

Figures 5 and 6 indicate that, in general, there is a 'sweet spot' where the canopy is not so long that the viscous drag becomes excessive (viscous drag accounts for close to 80% of the total drag of the preferred canopy), not so blunt at the front that the pressure drag increments too far to the point where the gradients may even cause separation in relatively calm conditions, and at a rearwards location where interference with the main

body is reduced. The final canopy length was based around the 3150–1300 canopy shape, however the rear taper was eventually extended marginally to assist in a smoother pressure recovery. It was finally moved further back to 'hang' off the back of the car (as discussed later).

Figure 6 Example of 'long' canopy configurations, pressure coefficient and turbulent kinetic energy surface contours. Quoted lift and drag values are for the canopy only (see online version for colours)
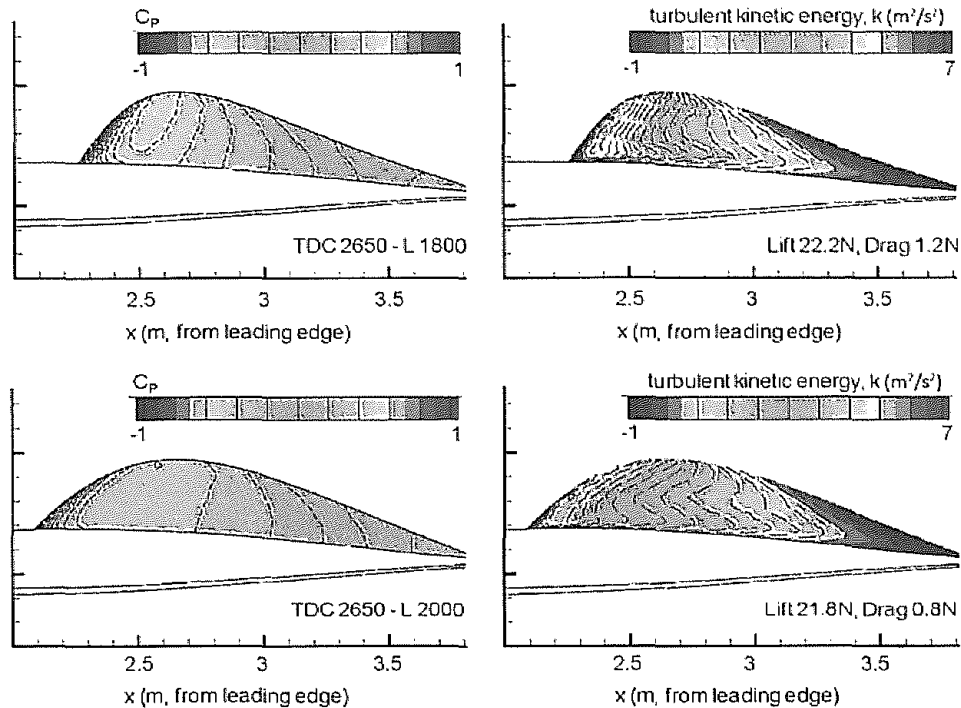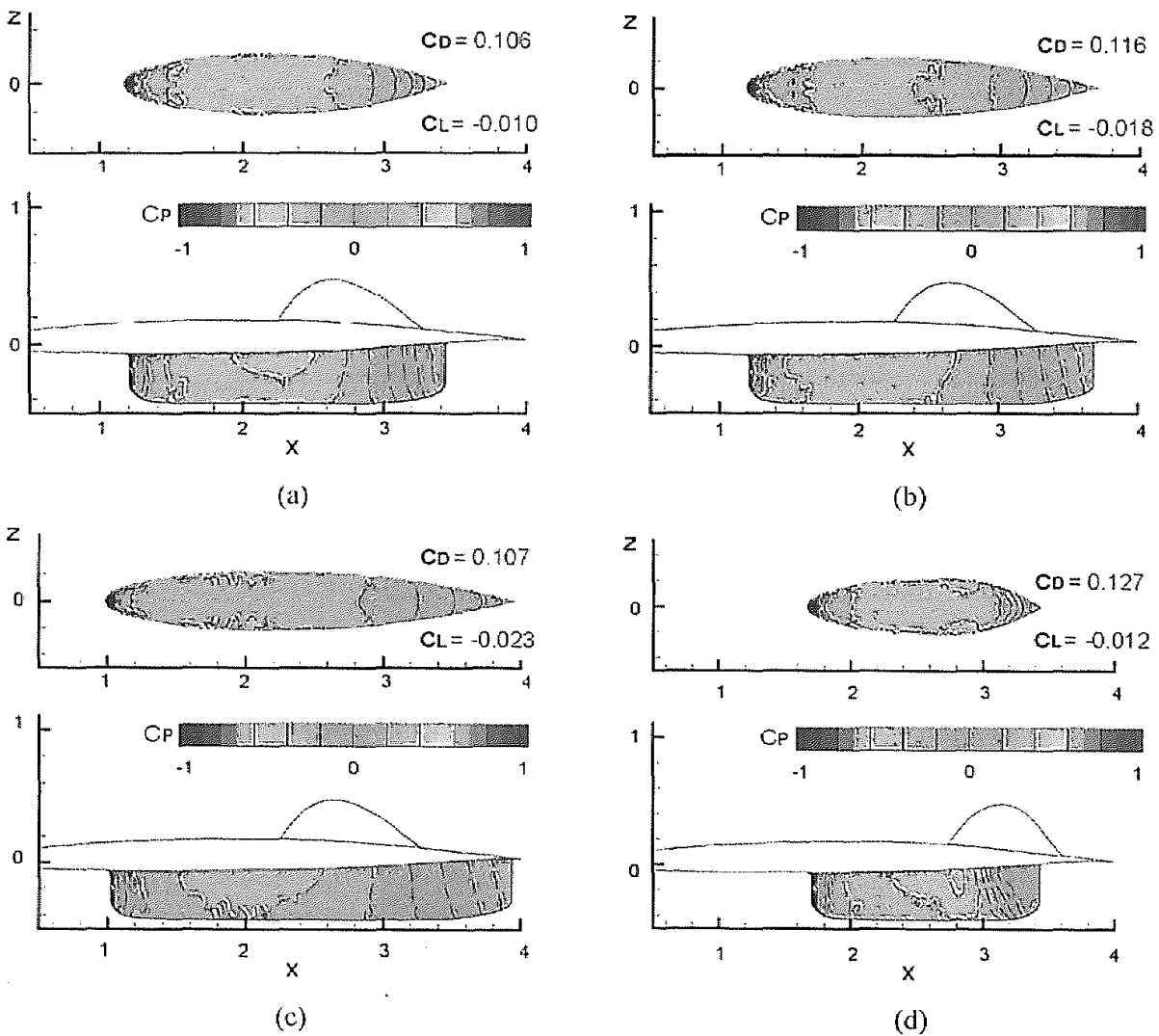

4 Bumpod

The design of the so-called 'bumpod' – the long fairing that encapsulates the volume of the driver that extends below the main car wing body – had to capture all feasible positions that could locate the driver with respect to the canopy locations already studied. The three main canopy locations of 2650, 2900 and 3150 mm from the leading edge were used to determine the longitudinal position of the bumpod. These were locked in by where the driver's hips would be located relative to the canopy and the 27° seating angle, such that the only parameters left to alter were the length of the bumpod and how much rear taper there should be. The leading edge profile was based on a symmetric NACA 66 series airfoil, and scaled accordingly so that it was wide enough at the hip point. Owing to this scaling the original aerodynamic data of the wing is invalid. However, the leading edge curvature of the bumpod was sufficient to maintain attached flow downstream. It was expected that viscous forces would dominate the bumpod's drag, however it could not be so short as to induce flow separation.

The bumpod length was referenced from the leading edge to the hip point (the widest point) as shown in the schematic of Figure 4; additionally the distance to the trailing edge was varied from 100 mm to 350 mm to 600 mm, effectively altering the rear taper ratio. Thus the three-number codes in Figure 7, for instance 2650_1030_600, refer to the

distance to the bumpods 'hip point' from the vehicle's leading edge, length from the 'hip point' to the trailing edge of the bumpod, and distance from bumpod trailing edge to the vehicle's trailing edge. Selected pressure coefficients are plotted in Figure 7, with full-car lift and drag data. Many other configurations were tested, however the important ones were the 3150–1220 and the 2650–1220 bumpod geometries placed 100 – 350 mm from the trailing edge. Both locations exhibited more consistent and predictable drag properties with speed compared to ones further forward on the main body, most likely for the same reasons as placing the canopy far back reduced its sensitivity by reducing interference with the main wing.

Figure 7 Contours of pressure coefficient around example bumpod configurations for 25 ms^{-1} car speed, annotated with full car aerodynamic coefficients: (a) 2650_1030_600; (b) 2650_1030_350; (c) 2650_1220_100 and (d) 3150_1220_600 (see online version for colours)

(a)

(b)

(c)

(d)

The 3150–1220 case had lower viscous drag as its bumpod was significantly smaller in wetted area, yet it was 'stumpier', increasing its pressure drag component thus giving a higher total drag – the finer but longer bumpods had a smaller pressure footprint (by 3–5%) despite their higher viscous drag.

The bumpod geometries with more abrupt taper feature stronger pressure gradients towards the rear, which means that the curvature is too sharp and the resulting adverse pressure gradient would tend towards flow separation, particularly in the presence of highly-disrupted flow coming off the rear wheel. Even without the wheel, the considerable increase in drag from the 2650_1030_600 example to the 2650_1030_350 variant in Figure 7 highlight this effect.

The 2650-1030-600 bumpod had the lowest C_{DX} and C_{LY} of the shapes tested and was therefore used as the basis for the latter stages of design. Eventually, with the canopy and bumpod being extended behind the trailing edge of the main body, the rear taper was extended slightly to further reduce the pressure gradient there, and other subtle modifications were introduced as will be discussed in Section 6.

5 Front wheel fairings

The actual fairing shape was not aerodynamically optimised in this design study, as it was designed for Sunswift III and proved effective; to save on design time as well as additional manufacture expense, it was retained for Sunswift IV. Thus the focus of the wheel fairing design centred on the location of the fairings with respect to the bumpod, with particular concern about the fairing/body junction vortex causing interference with the flow at the side rail of the car (i.e., vortices combining to augment drag in windy conditions). Having the fairings move with steering provides a small amount of 'power steering' from the aerodynamic side force effect, but more importantly allows the fairing to have a very low frontal area compared to typical competitor cars which have static large fairings wide enough to accommodate the maximum wheel angle; this contributes extensively to drag, especially in windy conditions where increased side-forces and prominent separation will be present.

Three longitudinal placements and three lateral placements were selected to determine the relationship of lift and drag, as per the schematic of Figure 8. The larger bumpod from the initial canopy study was used, as the wheel fairing placement would affect forces in a more exaggerated fashion and this allowed the fairing and bumpod optimisations to run in parallel development to save time. As the final bumpod was already anticipated to be shorter and further rearward, it was reasonable to assume the net drag would reduce further from the values seen in this study.

Figure 8 Parameters for wheel fairing position optimisation
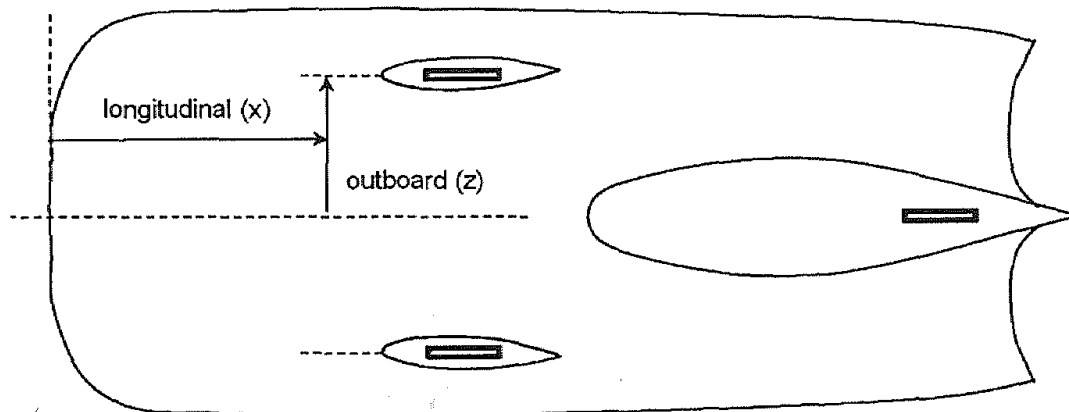
Space in the main body was required for suspension travel. Structurally speaking, a shorter distance between the suspension pick up points on the chassis and the wheel itself would make for a lighter more robust suspension; the further out the wheel, the longer it would have to be, and therefore heavier too, in order to take the stresses of a larger bending moment; this was considered on top of the pure aerodynamic analysis.

As the fairings move outward from the centreline, their pressure footprints on the underbody are contained at $z = 550$ and $z = 650$, whereas at $z = 750$ the lower pressure coefficient 'spills' up around the side rails of the car and thus influences the strength of the tip vortex. At the $x = 1150$ mm fairing placements the flowfield around the sides of the fairings and that around the bumpod is now 'joined' due to the narrower gap between them which in turn increases their effect on each other. The flow visualisation plane located half way between the ground and the underbody in Figure 9 shows the x-velocity component of the wake behind the fairings gets shorter the closer towards the bumpod they are placed, indicating flow being forced in a more lateral direction, increasing the overall disturbance and therefore overall drag. Around the fairings in particular, one can notice the increasingly strong and asymmetric acceleration of the flow around the fairings.

Figure 10 indicates that the further away from the bumpod the fairing was placed, the lower the overall drag of the car was. The closest the fairing was placed to the bumpod at $x = 1150$ mm, $z = 550$ mm resulted in the highest drag, as the compound flow acceleration between the fairings and bumpod resulted in a stronger velocity gradient, and therefore a stronger wake from both components. It also enhanced flow acceleration under the bumpod and fairings, increasing flow disturbance there. However drag was not the only concern; lift was also important in terms of avoiding additional downforce (primarily from increased flow under the bumpod) and at $x = 650$ mm fairing placement the lift is quite neutral (i.e., $C_{LY} \approx 0$), whereas the car has more downforce at $x = 150$ mm. This is partly due to the fairings acting as endplates, accelerating the air flow at the part of the car closest to the ground and causing some suction, but also due to the related enhanced pressure field around the bumpod.

There appears to be no straight line benefit in fairing placement at the most outboard location, and indeed this may have additional adverse affects when the car is in a cross wind, exaggerating the vortices produced by the fairing and the underbody. In a strong cross wind this could potentially migrate up and around to the top surface of the car, causing additional interference drag. Thus the slightly inboard location was reasoned to assist in keeping this vortex closely following the car underside. Also as the wheels/fairing are integrated and 'steer', keeping the fairing flush with the underside at all times is important. Leaving the fairing short of the side rail of the car made it possible to have more than $10°$ of steering lock. Therefore, for a good compromise on aerodynamic balance and practicality, the positioning around $x = 650$ mm was deemed to be the most suitable.


6   Full car optimisation

With the main components and layout established, considerable refinement of the design followed in quick order, relying increasingly on experience and intuition as the timeline precluded further parametric studies for variables other than yaw and pitch angles.

The following main decisions were taken:

- the lower airfoil surface (NACA 66-209) was re-profiled to be thinner and flatter to reduce sensitivity to ground effects; a conservative static −1.5 degree dive on wing for slight downforce (safety margin) was established as the 'standard' setup for the 2009 WSC for which the design would be largely untested on the road

- 2° 'toe-in' on wheel fairings was incorporated to get very mild 'sail' out of them; considerable front corner rounding to minimise sharp angles producing strong vortices or separation in yaw was included

- the side rails were further rounded and the array surface angled to similarly limit adverse effects in yaw – side rails profiled to minimise 'tip vortices' from air drawn to the upper surface.

The canopy and bumpod chamfers were also adjusted, and the bumpod was given a slight draft angle for ease of mould release. Further, the leading edge was given a sweep angle from the main body to reduce the severity of the junction and to give the car a more purposeful stance – testing revealed that any higher angles tended to direct excessive flow to the underside where the wheel causes flow disruption and therefore additional drag. Finally, the so-called 'Bat-Wing' trailing edge was introduced. A comparison of the original baseline design used for most of the parametric studies, next to the final car at the point of design-freeze, is shown in Figure 11.

Figure 9 X-velocity contours on the mid-plane between car body and ground, for fairing x-locations at $z = 650$ mm (see online version for colours)
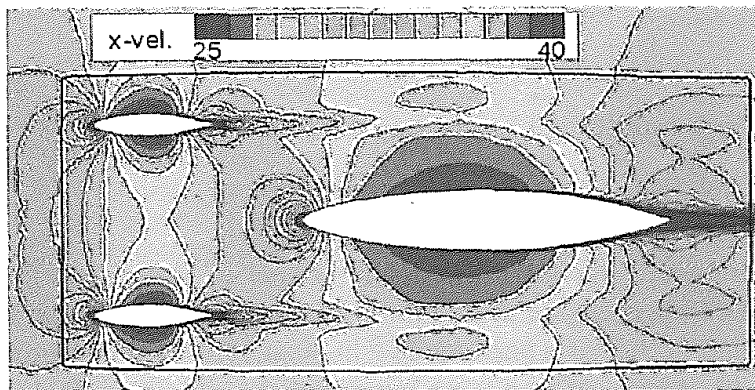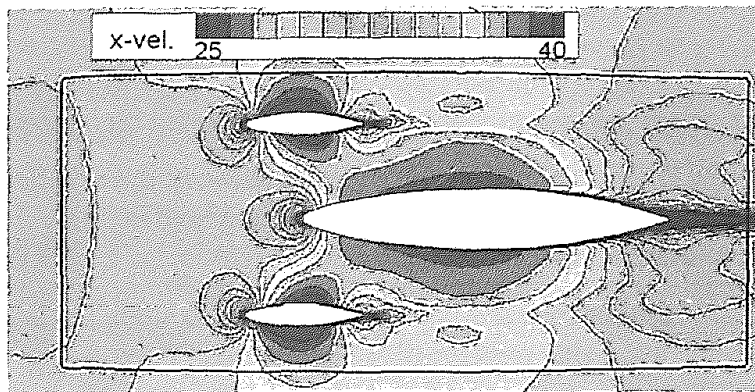

(a)
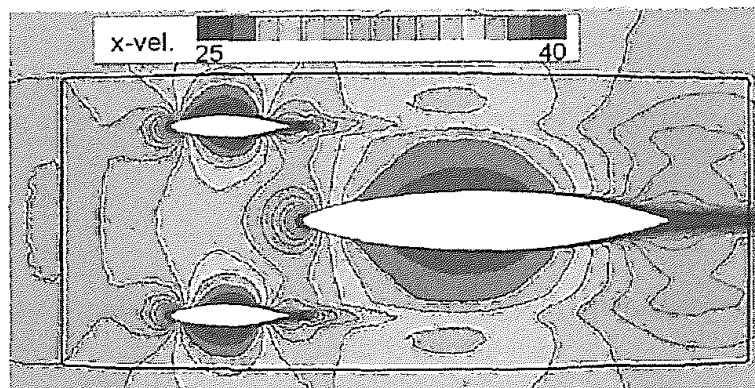
(b)

Figure 9 X-velocity contours on the mid-plane between car body and ground, for fairing
x-locations at z = 650 mm (see online version for colours) (continued)
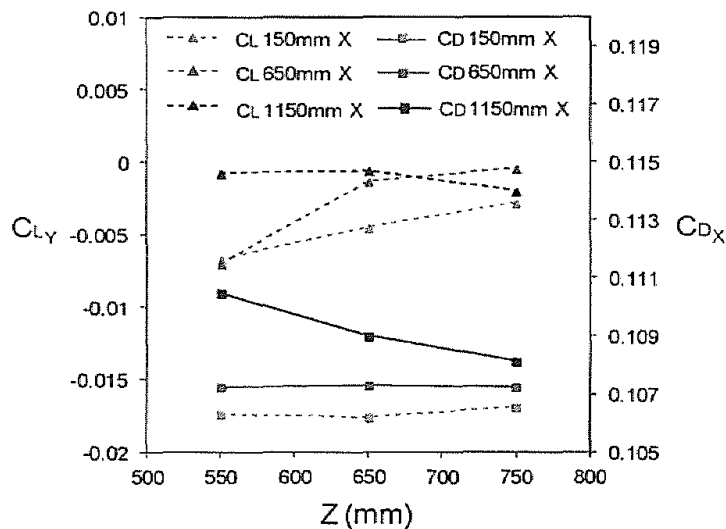

(c)

Figure 10 Full car lift and drag coefficients for fairing locations at a car speed of 35 ms^{-1}

These modifications were introduced over the course of just a few design evolutions, following which a comprehensive evaluation of the car in pitch and yaw was completed to create an aero map of the car's performance in most conceivable conditions.

0, 10, 20 and 30 degrees of yaw were investigated at 70, 90, 110, 130 and 200 km/h, with 0° and 10° representing the most typical conditions. The higher speeds were designed to simulate cases of some headwind or gusts (for instance car at 100 km/h, oncoming wind at 30 km/h) and an extreme gust loading to ensure under no one-off circumstances would the car become airborne. Pitch sensitivity was also analysed as well as performance with steering angle for the front fairings but will not be covered in depth here for the sake of brevity.

6.1   Aerodynamic forces

The data in Figure 12 shows the drag coefficient for the car from 0° to 30° wind yaw angles (i.e., the car maintains its x-oriented direction as it would have to on the road) for the given velocity range. C_{DX} tends to reduce with increasing velocity, with a value of about 0.11 for the car at normal cruising speed; in nomenclature more familiar to

designers of bluff automotive bodies, the C_{DA} (C_{DX} multiplied again by frontal area) predicted by the simulations of the final configuration at cruising speed (90 km/h) is 0.085 m². The contribution of the total drag from the viscous and pressure components are 28% and 72% respectively, and this varies little (<2%) across the whole speed range tested for zero yaw, indicating no onset of significant separation at higher velocities.

Figure 11 (a) The original baseline configuration for optimisation studies and (b) the final vehicle following further refinement (see online version for colours)
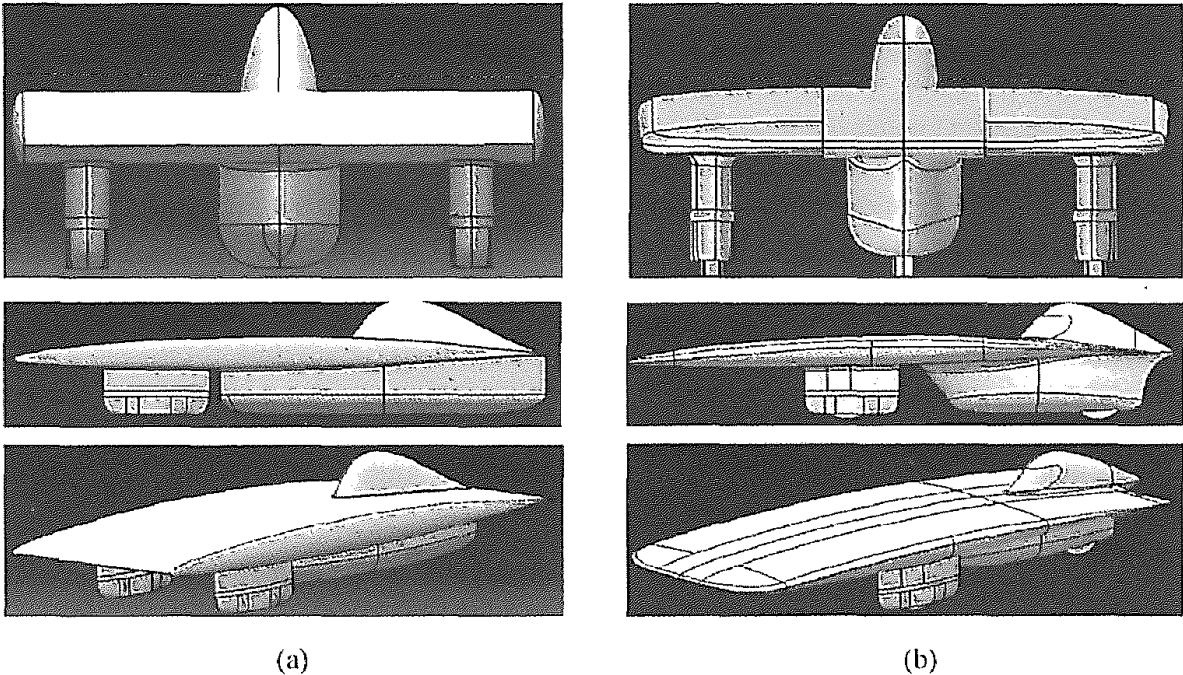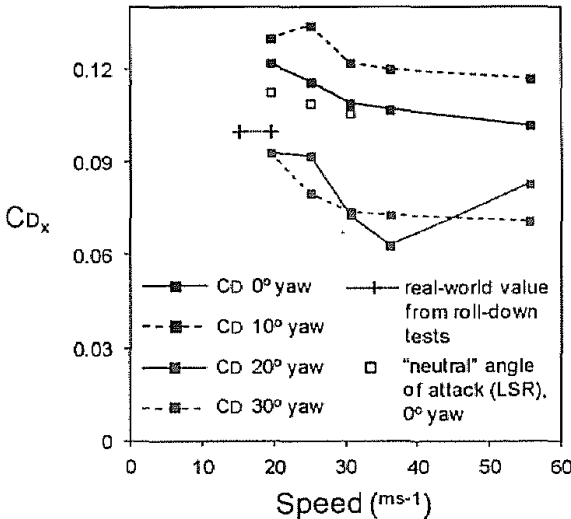

(a)   (b)

**Figure 12** Drag coefficient for final configuration in yaw conditions for various car plus wind speeds

The similar profiles for 0° and 10° indicate that the flow remains generally well-attached and under control in mild side wind conditions, while at more extreme wind angles a high level of flow separation occurs which reduces C_{DX} and shifts the emphasis onto a high side force – this effect is often presumed to be a reduction in drag

due to a 'sailing' effect (Tamai, 1999), however the retarding force simply acts in a more complex way than a pure x-direction component. The car will certainly not have less total drag operating in a crosswind.

Figure 12 also demonstrates that the car at an approximately neutral angle of attack, which was the configuration used for the solar-powered Land Speed Record in 2010 and in qualifying for the 2011 WSC, features a drag reduction of around 5% at cruising speed (90 km/h) compared to the original configuration. This highlights the importance of fine-tuning the setup; with confidence gained through real-world testing, small changes can make a considerable difference while maintaining a safety margin. Rolldown testing in fairly controlled conditions in 2011 produced the real-world average value indicated on Figure 12, though it must be noted that the data scatter was relatively high in that instance. Nevertheless, it is likely that a large proportion of the 15% difference between the CFD and the real-world testing is as a result of the amount of laminar flow present on the actual car at speed. Only further testing would provide a more comprehensive basis for correlation, however the car clearly lives up to its low-drag expectations from the digital design process. The numerical results indicate that close to 70% of the car's total drag is from the viscous component when the flow is fully-attached.

The lift coefficients in Figure 13 show the downforce generating ability of the car at its original $-1.5°$ nose-down angle, exhibiting a desirable tendency to produce a stronger force at more extreme conditions such as high transient gusts and the onrush of air from passing road trains; the car is highly unlikely to lift off or suffer destabilising loss of grip under such circumstances.

Figure 13 Lift coefficient for final configuration in yaw conditions for various car plus wind speeds
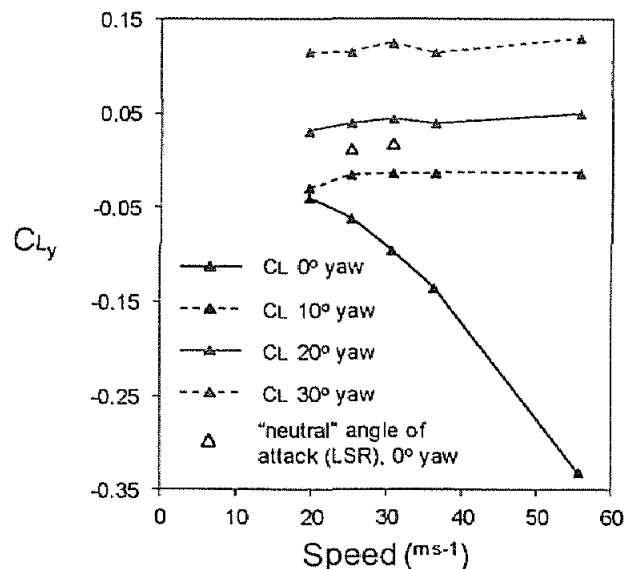

The main body produces lift, though this is more than offset by the downforce of the bumpod which operates in extreme ground effect. At a neutral angle of attack, the lift force is similarly close to neutral (reflecting the dominance of the main wing body sensitivity to pitch), tending towards mild lift production at higher speeds. It is therefore not recommended to run the car in this condition during the race, but under the low-wind, highly-controlled conditions of the Land Speed Record, such a setup allowed for minimal

rolling resistance and more swift acceleration, the equivalent of taking over 10kg of weight out of the car.

An increase in C_{LY} occurs when the car is in yaw, with positive total lift being produced at 20° and 30°. In part this is due to the disruption of flow around the main wing due to separation of flow around the front wheel fairings and bumpod, and the higher pressure acting on the surfaces of these components which the oncoming air 'sees' with a more oblique angle. At the same time, the flow over the upper surface remains largely attached but the z-component of the air flow means that the effective chord of the wing section is increased, producing more low pressure than previously. If the wing did not have a mild built-in downforce, these rare conditions would produce excessive lift and destabilise the vehicle. The side force behaviour of the vehicle as plotted in Figure 14 shows that the car has quite predictable characteristics in windy conditions. At the lower end of the cruising speed rage (up to around 30 ms^{-1}), the side force coefficient does not change significantly enough to cause sudden steering corrections to be made in a gust, though the wheel fairings and bumpod act as asymmetric wings to produce a non-trivial force. At higher combined flow speeds (car plus wind) the side force component becomes more sensitive and critical, and would cause the car to 'crab' and require considerable steering input to hold course. Fortunately such events would be short and controllable, and the steering angle on the fairings would instantly reduce the effect by reducing their effective angle of attack as well as their drag. The effect of separated flow from front fairings interacting with the bumpod is discussed in the following section.

Figure 14 Side force coefficient for final configuration in yaw conditions for various car plus wind speeds
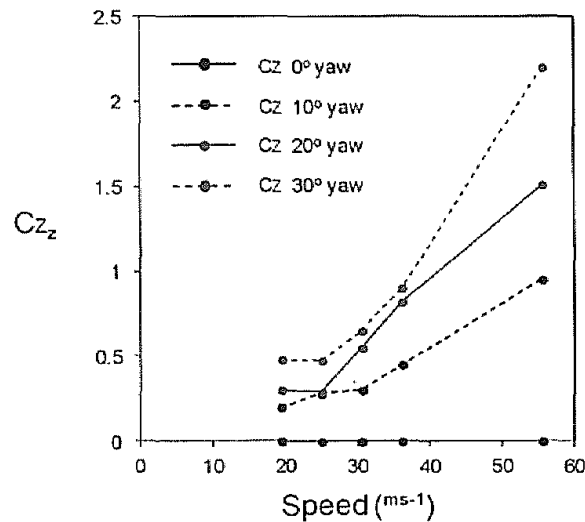
6.2 Further analysis

Figure 15 presents digital oil-flow pathlines for a speed of 30 m s^{-1}, as calculated next to the body surface to yield visualisation similar to that commonly obtained from wind tunnel tests. When there is no cross-component of flow, the top-down plan view of the car shows that the flow is completely attached with mild disturbance from the canopy and essentially no spillage of flow from the underside around the side rails. Underneath the car the much larger disturbance caused by the bumpod is clear, though the flow remains attached and smooth. The downstream path of the vortices from the front wheel

fairing/body junction (see Figure 16) shows the low pressure from the bumpod draws them inboard of the side rails, preventing them from interfering with the vortices there but creating slightly messier flow at the trailing edge.

At 10°, the flow is essentially still attached to the majority of the car apart from the leeward side of the canopy towards the trailing edge, although the increasing vortex strength around both the canopy and bumpod can be seen. At higher angles of yaw this separation and vortex roll up is more noticeable on the top surface, to the point at 30° where the canopy suffers large-scale flow separation, though the attachment line is drawn to the top of the trailing edge to provide some measure of control over where the flow leaves the vehicle.

As the flow yaw angle increases beyond 10°, the windward wheel fairing shields the bumpod to an extent and features less disturbance in the wake compared to the leeward fairing which has a large wake which at 20° appears to leave the bounds of the underside of the car, while the low pressure on the suction side of the fairing simultaneously draws flow down from the upper surface. At the highest angle of 30° the flow around all protrusions is highly separated and the windward wheel fairing has stalled almost completely, although this flow is blocked quite neatly by the bumpod, ensuring that the disruption to the rest of the flowfield is minimised and the bumpod itself does not suffer excessive separation other than on its underside. The leeward wheel fairing appears to act as a turning vane for the leeward side of the bumpod, ensuring the oncoming flow is 'deflected' towards the bumpod, minimising the flow disruption there.

To help visualise the three-dimensional flowfield, the off surface flow structures shown in Figures 16 and 17 are iso-surfaces of velocity at 15 m s^{-1} (50% of the freestream velocity). This provides an exaggerated view of areas of major flow disruption, separation or wake. For no wind yaw there is very little low speed flow that extends a significant distance from the rear of the car, indicating the flow quality is good and separation is minimal. Wake regions are narrow and controlled, with small vortices close to the car surface.

From Figure 16, as wind yaw increases to 10° the first obvious point of separation and flow disruption is from the wheel/ground region, with a significant vortex forming from the rear of the canopy too. At 20° the larger-scale separation around the fairings and bumpod is clear, with the side-rail vortex on the leeward side leaving the car at two distinct points: at the x-position of the front fairings due to their influence, and again towards the trailing edge. As indicated by the previous oil-flow figures, at 30° the flow is totally separated around the fairings and a large part of the bumpod, as well as at the rear of the canopy. The iso-surfaces extend far enough away from the body that the mesh becomes quite coarse, indicating that the extent of these wakes (and therefore the total side force) may be over-predicted.

Figure 17 confirms that at 0° and 10° the major vortices are essentially contained within the bounds of the car. The 20° and 30° images for the car underside further highlight the way in which the windward fairing shields the bumpod from excessively high oncoming flow velocities, and the bumpod blocks and re-aligns some of the separated flow from the fairing. This figure also confirms to a certain extent that the so-called 'batwing' concept at the trailing edge works reasonably well in providing the flow with well-defined points at which to leave the car in difficult flow conditions.

Figure 15 Numerical oil flow visualisation on the upper (left) and lower (right) surfaces for various yaw angles for car travelling at 25 m s^{-1} (90 km/h)
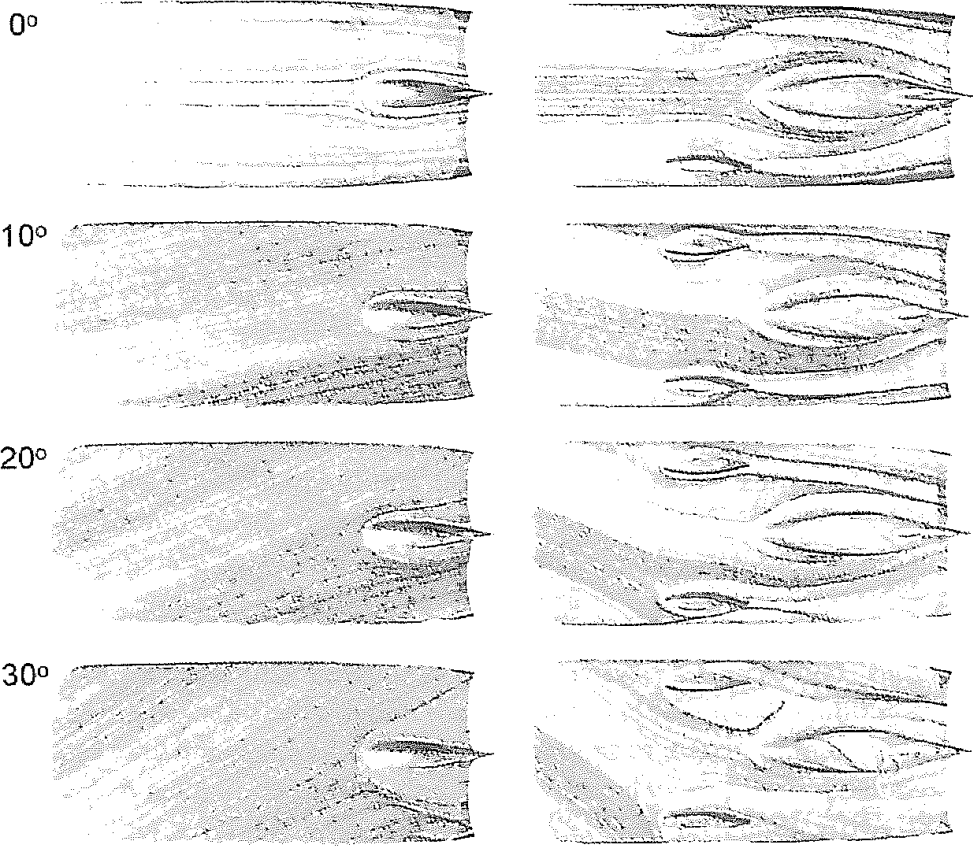
0°

10°

20°

30°

Figure 16 Side view of off-body vorticity iso-surfaces for various yaw angles at 30 m s^{-1}
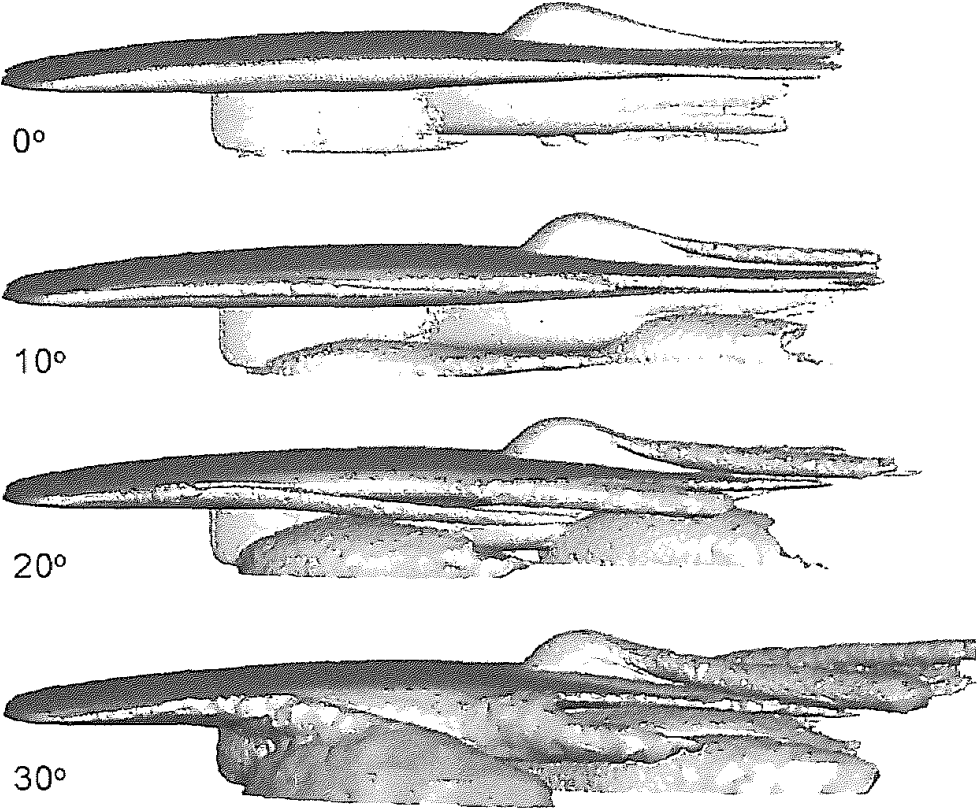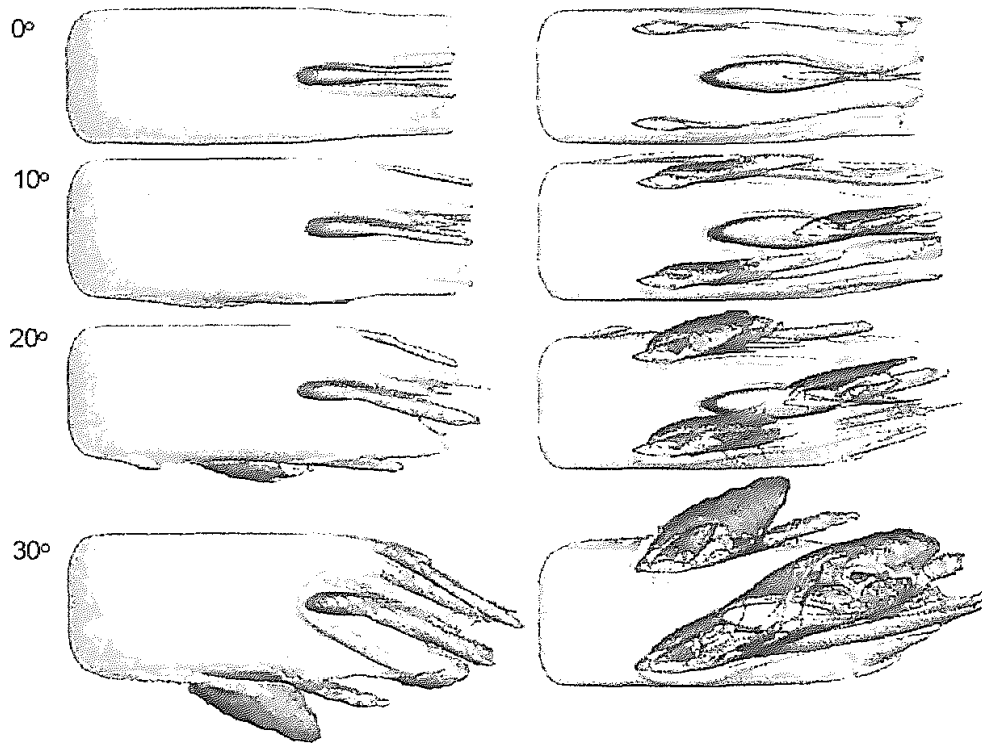
0°

10°

20°

30°

Figure 17 Top (left) and bottom (right) views of off-body vorticity iso-surfaces for various yaw angles at 25 m s^{-1}

7 Notes on real-world performance

Aside from the quantitative figures from testing presented for drag coefficient in Figure 12, feedback from the experienced drivers in both 2009 and 2011 was that the car was fast in a straight line as well as remarkably stable in windy conditions. In situations where the support vehicles were being buffeted heavily in 2009, the solar car itself was predictable and rarely affected. The car's silicon-class-winning WSC performance in 2009 was analysed by the authors, with particular focus on days 3 and 4 when extremely windy conditions were encountered and cars were in general running below top performance as a result. Sunswift IV managed an average speed of 78.4 km/h in this period, approximately equal to the average speed of the 2nd placed Nuna car – with its 11% more efficient array – and was able to average close to 8km/h faster than MIT's entry, the next-fastest silicon-array vehicle. Sunswift IV's ability to offer low-drag, predictable and controlled aerodynamic performance in challenging meteorological conditions was validated.

The Guinness World Land Speed Record was set at a speed of 88.8 km/h on the 7th of January 2011, at around 10:30AM. The previous long-standing record (GM Sunraycer's 78 km/h on 1.5kW) was broken on what was unfortunately a quite cloudy morning at HMAS Albatross Naval Base, with Sunswift IV drawing a peak of around 1.05 kW from the array exiting the measured 1000 m in both directions (the batteries were removed to comply with regulations). Extrapolations indicated that the car would be capable of close to 100 km/h at 'solar noon' on maximum array power of around 1.35 kW with an optimal setup. As a pure test of straight-line aerodynamic efficiency, the record is a crowning achievement for the vehicle.

8 Conclusion

The aerodynamic design of the Sunswift IV solar-powered car was conducted entirely in the digital domain purely out of cost and time considerations. Out of this programme, a highly optimised vehicle resulted; one which has proven to be one of the most successful solar-powered vehicles yet built, winning its class in the 2009 and 2011 World Solar Challenges and setting a new land speed record for solar-only power in 2011. Parametric studies of geometric aspects of the main components of the vehicle established an efficient basic design which was then refined extensively to produce a vehicle with a predicted C_{DX} of 0.11 (and a C_{DA} of 0.085 m^2) in idealised flow conditions for a conservative race setup, and approximately 0.10 for a lift-neutral configuration. Assuming a reasonable run of laminar flow on the actual vehicle, particularly on the underside, the real-world C_{DX} of the vehicle was found in controlled testing to be closer to 0.09.

However, from the beginning, the philosophy was to design an effective shape for handling challenging crosswinds and gusts. The ability to conduct CFD simulations on the car for a wide variety of wind conditions and car pitch angles proved to be invaluable in refining the design until attached flow could be maintained in most conditions. In more extreme winds, the alignment, shape, and relative proximity of the front wheel fairings and the bumpod in particular proved, in concert with a well-rounded leading edge and side rails, to be remarkably effective in meeting and guiding the oncoming air around the car in a manner which minimised drag and the amount of steering input required.

The project in general confirmed that using computational fluid dynamics is a viable means of designing a vehicle without having to use a wind tunnel. However, great care must be taken in setting up and analysing the results; the vehicle's optimal setup was only established over a year after its first race outing thanks to extensive real-world testing which allowed some of the conservatism of the original angle of attack to be pared back, coupled with improvements to suspension and control. The team spent 2013 working on a radically different car, Sunswift 'eVe', which featured four wheels and a passenger seat, making it a more practical and relatable vehicle that continued the spirit of innovation and achievement that is the hallmark of the team. The car took line honours as the fastest Cruiser Class vehicle in the 2013 World Solar Challenge.

References

Abbott, I. and von Doenhoff, A.E. (1959) *Theory of Wing Sections*, Dover Publications, Mineola, New York, USA.

Arkesteijn, G.C.M., de Jong, E.C.W. and Polinder, H. (2007) 'Loss modelling and analysis of the Nuna solar car drive system', *Int. Conf. On Ecologic Vehicles and Renewable Energies*, Monaco, pp.1–10.

Barber, T.J., Leonardi, E. and Archer, R.D. (2002) 'Causes for discrepancies in ground effect analyses', *The Aeronautical Journal*, Vol. 106, No. 1066, pp.653–657.

Boulgakov, A. (2011) *Sunswift IV Strategy for the 2011 World Solar Challenge*, Thesis submitted as a requirement for the degree Bachelor of Engineering (Electrical Engineering), The University of New South Wales, Australia.

Cusack, M.J., Prehn, J.G. and Mavriplis, C. (1997) 'Aerodynamic design of the George Washington university solar car sunforce 1', *Int. J. of Vehicle Design*, Vol. 18, No. 2, pp.213–232.

Diasinos, S. (2009) *The Aerodynamic Interaction of a Rotating Wheel and a Downforce Producing Wing in Ground Effect*, PhD thesis, University of New South Wales, Australia.

Diasinos, S., Barber, T.J. and Doig, G. (2013) 'Influence of wing span on the aerodynamics of wings in ground effect', *Proc. IMechE Part G: Journal of Aerospace Engineering*, Vol. 227, No. 3, pp.564–568.

Doig, G. and Barber, T.J. (2011) 'Considerations for numerical modeling of low aspect ratio inverted wings in ground effect', *AIAA Journal*, Vol. 49, No. 10, pp.2330–2333.

Doig, G., Barber, T. and Neely, A. (2011) 'The influence of compressibility on the aerodynamics of an inverted wing in ground effect', *ASME J. Fluids Eng.*, Vol. 133, No. 6, pp.1–12.

Fluent Inc. (2006) *Fluent User Guide*, Available from http://www.ansys.com, PDF file.

Himeno, R. and Matsubara, T. (1994) *Aerodynamic Drag Reduction of a Solar Car using CFD*, SAE 94A1027, Warrendale, PA.

Hoerl, A., Larson, D.K., Stenson, M.S., Dennis, K.D. and Suzen, Y.B. (2008) *Aerodynamic Design Improvement of NDSU Solar Car through Computational Fluid Dynamics*, SAE 2008-01-2251, Warrendale, PA.

International Solarcar Federation (2010) *World Solar Car Challenge Technical Regulations for the 2011 Event*, pp.1–15, http://www.worldsolarchallenge.org/files/78_paticipants_regulations _technical-regulations.pdf

McManus, J. and Zhang, X. (2006) 'A computational study of the flow around an isolated wheel in contact with ground', *Journal of Fluids Engineering*, Vol. 128, No. 3, pp.520–530.

Pudney, P. (2000) *Optimal Energy Management for Solar-powered Cars*, Thesis submitted as a requirement for the degree Doctor of Philosophy, The University of South Australia, Australia.

Roche, D.M., Schinckel, A.E., Storey J.W., Huphris, C.P. and Guelden, M.R. (1997) *Speed of Light: The 1996 World Solar Challenge*, UNSW Photovoltaics Special Research Centre, Sydney, Australia.

Shih, T.H., Liou, W.W., Shabir, A., Yang, Z. and Zhu, J. (1995) 'A new k-e Eddy viscocity model for high reynolds number turbulent flows', *Computers Fluids*, Vol. 24, No. 3, pp.227–238.

Taha, Z., Passarella, R., Sugiyono, Rahim, N.A., Sah, J.M. and Ahmad-Yazid, A. (2011) 'CFD analysis for Merdeka 2 solar vehicle', *Advanced Science Letters*, Vol. 4, Nos. 8–10, pp.2807–2811.

Tamai, G. (1999) *The Leading Edge: Aerodynamic Design of Ultra-Streamlined Land Vehicles*, Bentley Publishers, Cambridge, MA, USA.

Yang, Y. and Liou, W.W. (2005) *Comparison of Computational and Experimental Aerodynamics Results for a WMU Solar Car Model*, SAE 2005-01-1910, Warrendale, PA.

Nomenclature

C_{DX}	Coefficient of force in the x-direction based on frontal area (drag)
C_{DY}	Coefficient of force in the y-direction based on frontal area (lift)
C_{DZ}	Coefficient of force in the z-direction based on side area (side force in yaw)
C_{DA}	Coefficient of drag area (m^2)
C_P	Coefficient of pressure
D	Drag force (N)
L	Lift force (N)
P	Power (W)
v	Vehicle speed (ms^{-1})

CAD	Computer-aided design
CFD	Computational fluid dynamics
DC	Direct current
LSR	Land speed record
UNSW	The University of New South Wales
WSC	World Solar Challenge